NJC

ROYAL SOCIETY OF CHEMISTRY

PAPER

View Article Online
View Journal | View Issue

Cite this: *New J. Chem.*, 2021, 45, 21569

Metal phosphide CuP_2 as a promising thermoelectric material: an insight from a first-principles study†

Un-Gi Jong, *[a] Chol-Hyok Ri,[a] Chol-Jin Pak,[a] Chol-Hyok Kim,[a] Stefaan Cottenier [b] and Chol-Jun Yu *[a]

Received 28th July 2021,
Accepted 26th October 2021

DOI: 10.1039/d1nj03624f

rsc.li/njc

In the search for better thermoelectric materials, metal phosphides have not been considered to be viable candidates so far, due to their large lattice thermal conductivity. Here we study the thermoelectric properties of metal phosphide CuP_2 in the monoclinic phase using first-principles calculations based on self-consistent phonon theory and electron Boltzmann transport theory. Our lattice dynamics calculations reveal that CuP_2 exhibits Cu-dimer rattling modes, which strongly scatter the heat-carrying acoustic and low-lying optical phonons, resulting in an unusually low lattice thermal conductivity below 3.6 W m^{-1} K^{-1}, being about a half of the conventional thermoelectrics GeTe. We predict Seebeck coefficients, the value of which at 300 K is in good accordance with the experiment, and power factors that are superior to the conventional thermoelectrics GeTe, possibly due to flat- and dispersive-band structures with high orbital degeneracy. Finally, we assess its thermoelectric performance by evaluating the figure of merit *ZT*, finding that upon p-type doping *ZT* can reach over 1.3 at a high temperature of 700 K by optimizing the hole concentration. Our results highlight the potential of using metal phosphide CuP_2 as a promising material for thermoelectric applications with practical performance and low cost.

1 Introduction

Searching for new thermoelectric materials (TMs) has attracted significant attention in applications of waste heat recovery, power generation and refrigeration, as TMs directly interconvert heat and electricity.[1–4] Their thermoelectric conversion efficiency at a given temperature T is determined by a figure of merit $ZT = S^2\sigma T/(\kappa_l + \kappa_e)$, where S is the Seebeck coefficient, σ is the electrical conductivity, and κ_l and κ_e are the lattice and electron thermal conductivities, respectively.[5] For commercial applications, TMs are required to have higher *ZT* over 1 within a wide range of temperatures, together with low cost, non-toxicity and long-term stability under ambient conditions.

These requirements were met in chalcogenides,[2,6–17] Bi–Te alloying systems,[18–25] skutterudites (Co, Ni)As_3,[26–31] Si–Ge alloys,[32,33] *etc.* For a typical example, Bi_2Te_3 was reported to have a relatively high peak *ZT* over 1.2 at room temperature, which is due to its lower κ_l and higher carrier mobility through Sb doping, by Deng *et al.*[20] In particular, a remarkably high *ZT* of ~2.3 around 700 K was found in lead-free chalcogenide GeTe systems by Hong *et al.*, which was achieved by decreasing the phase transition temperature and introducing a resonant energy level *via* Sb and In co-doping.[11] In addition to these conventional TMs, some oxides,[34–37] halide perovskites[38–40] and metal phosphides[41–43] have also emerged as promising candidates for thermoelectric applications. These are known as unconventional TMs, being composed of chemically inert and earth-abundant elements, which lead to low cost and highly stable devices under ambient conditions. For realistic thermoelectric applications with them, however, their thermoelectric efficiencies should be improved so as to provide a high *ZT* over 1. In fact, large-scale power generation and refrigeration by using TMs are not very practical owing to the shortage of constituent elements in flagship materials such as Bi_2Te_3[18,19] and GeTe[11] and the limited *ZT* of more sustainable alternatives.

[a] *Chair of Computational Materials Design (CMD), Faculty of Materials Science, Kim Il Sung University, Pyongyang, PO Box 76, Democratic People's Republic of Korea. E-mail: ug.jong@ryongnamsan.edu.kp, cj.yu@ryongnamsan.edu.kp*

[b] *Department of Electromechanical, Systems and Metal Engineering & Center for Molecular Modeling (CMM), Ghent University, Technologiepark-Zwijnaarde 46, Gent BE-9052, Belgium*

† Electronic supplementary information (ESI) available: Figures for comparison of phonon dispersions calculated using 2 × 2 × 2 and 3 × 3 × 3 supercells, SCP dispersion curves at different temperatures, lattice thermal conductivity as a function of the *q*-point mesh, average phonon lifetime τ_{3rd} and group velocity v_g, electronic band structures computed with and without the SOC effect, the convergence test of estimating *ZT* according to the size of the *k*-point mesh, comparison of *ZT* calculated with the PBE and mBJ functionals or with various relaxation times for CuP_2. See DOI: 10.1039/d1nj03624f

In the past, phosphides were usually disregarded in most of the thermoelectric studies as the heavy and scarce elements of Te, Se or Sb were believed to be the key to attaining both low κ_l and good electronic transport properties.[2,6–14,18–25,44] However, as Qi *et al.*[43] reported recently, copper phosphide CuP_2 with a single crystalline (polycrystalline) structure has a much lower lattice thermal conductivity κ_l of 3.57 (0.62) W m^{-1} K^{-1} than the prototypical TM GeTe, which has κ_l of 6.96 W m^{-1} K^{-1}[45] (2.80[46]) at 300 K. Moreover, Odile *et al.*,[42] in the late 1970s, observed a high Seebeck coefficient of 692 μV K^{-1} at room temperature, which is also much superior to the value of GeTe (29 μV K^{-1}).[11] From such considerations, we conceive the copper phosphide CuP_2 to be the latent thermoelectric material satisfying the desired terms for practical applications, such as high performance, low cost, non-toxicity and high stability. In spite of extensive efforts in finding new TMs, only a few studies have been conducted for lattice transport and thermoelectric properties of CuP_2 so far,[42,43] resulting in a lack of comprehensive insight into its thermoelectric performance. In this work, with the purpose of exploring novel TMs, we perform first-principles investigation of anharmonic lattice dynamics and thermal transport properties of metal phosphide CuP_2 in a monoclinic phase with space group $P2_1/c$, revealing its promising thermoelectric performance.

2 Computational methods

Within the density functional theory (DFT) framework, the calculations were performed by using the pseudopotential plane-wave method as implemented in the Vienna *Ab initio* Simulation Package (VASP).[47,48] The projector augmented wave (PAW) potentials[49,50] provided in the VASP code, where the valence electron configurations of elements are given as Cu-3d^{10}4s^1 and P-3s^{2}3p^3, were used for interaction between ionic cores and valence electrons. The Perdew–Burke–Ernzerhof (PBE) functional within the generalized gradient approximation (GGA)[51] was used for exchange–correlation interaction among the valence electrons. Convergence testing suggested that a plane-wave cutoff energy of 600 eV and a Γ-centered (10 × 10 × 8) k-point mesh were sufficient to converge the total energy within 3 meV per unit cell containing 12 atoms. Atomic force and total energy convergence thresholds were set to 10^{-3} eV Å^{-1} and 10^{-8} eV, respectively. For the 2 × 2 × 2 supercell (96 atoms) calculations for lattice dynamics, we applied the same convergence thresholds but reduced the cutoff energy and k-point mesh to 400 eV and (5 × 5 × 4), respectively.

In the calculation of the electronic band structure, density of states (DOS) and electronic transport properties, we applied the modified Becke–Johnson (mBJ) exchange[52] plus the PBE correlation functional, which is known to give highly accurate results, being close to the HSE06 hybrid functional[53] or GW[54] calculations, with much less computational efforts. Relativistic effects were considered by treating the spin–orbit coupling (SOC) explicitly.

To proceed with the calculation of electronic transport properties, we first determined the relaxation time of electron τ as a function of temperature in CuP_2 by using the deformation potential theory (DPT). In this method, the carrier mobility μ is estimated by considering the influence of acoustic phonon modes on the electronic bands with the following formula,[38,55,56]

$$\mu = \frac{(8\pi)^{1/2}\hbar^4 eC}{3(m^*)^{5/2}(k_B T)^{3/2}D^2} \quad (1)$$

where C, D, T, m^*, e, k_B, and $\hbar$ are the elastic constant, deformation potential, temperature, effective mass of electron, electron charge, Boltzmann constant, and reduced Planck constant, respectively. Considering the relation $\mu = e\tau/m^*$, therefore, the relaxation time τ can be expressed as follows,

$$\tau = \frac{(8\pi)^{1/2}\hbar^4 C}{3(m^* k_B T)^{3/2}D^2} \quad (2)$$

Here, the deformation potential D can be easily obtained by computing the shifts of conduction band minimum (CBM) by dilating and compressing the unit cell volume. Then, the electronic transport properties were quantitatively investigated by solving the semi-classical Boltzmann transport equation (BTE) as implemented in the BoltzTrap2 code.[57] With this code, we calculated the electrical conductivity, Seebeck coefficient and electronic thermal conductivity within the constant relaxation time approximation (CRTA), where the relaxation time is fixed to be a single and isotropic value. In these calculations, a denser k-point mesh of (24 × 24 × 16) for the Brillouin zone (BZ) integration was utilized.

Phonons can be calculated in the harmonic, quasi-harmonic and anharmonic approaches, where every step is more accurate than the previous one. To determine the lattice thermal conductivity, one should solve the phonon BTE within CRTA, which requires accurate anharmonic force constants (IFCs) to the 3rd-order at least. We applied the anharmonic approach in a direct way to perform lattice dynamics, as implemented in the ALAMODE code.[58,59] In this approach, IFCs are computed by utilizing the compressive sensing lattice dynamics, which is highly efficient in the computation of phonon dispersion relations based on the finite displacement of all atoms in a supercell.[60,61] The 2 × 2 × 2 supercells were used to extract both the harmonic and anharmonic IFCs of monoclinic CuP_2. We displaced the relevant atoms from their equilibrium positions by 0.01 Å considering the crystalline symmetry, and then calculated atomic forces for each displaced configurations, extracting the harmonic IFCs. In order to include the anharmonic effects, we performed self-consistent phonon (SCP) calculations at finite temperatures up to 1000 K. For these calculations, we prepared over 80 configurations allowing all of the atoms to be moved randomly with large displacements,[60] and calculated the atomic forces for each configuration using precise DFT calculations. The cutoff distances were set to 4.8, 3.7, 2.7 and 2.7 Å for the 3rd-, 4th-, 5th- and 6th-order IFCs, while the higher order IFCs were restricted to the three-body terms. With the higher-order IFCs, the relative errors were guaranteed to be below 4.5%, being sufficient for fitting the atomic forces to the DFT-calculated ones. By using the calculated 3rd-order IFCs,

we solved the phonon BTE within CRTA to calculate the lattice thermal conductivity.

3 Results and discussion

3.1 Crystallographic structure

Prior to studying the lattice and electronic transport properties, we briefly survey the crystallographic structure of metal phosphide CuP_2. According to previous experiments,[42,43,62] it crystallizes in a monoclinic phase with a $P2_1/c$ space group. In Fig. 1(a), we show the unit cell of the monoclinic CuP_2 crystal, optimized by using PBE, where Cu atoms form a dimer and occupy the center of the CuP_4 tetrahedron. The crystal structure is characterized by a layered configuration, in which Cu layers and P networks in the *bc*-plane repeat alternatively along the *a*-axis. In this work, the lattice constants were determined with a PBE functional as a = 5.81 Å, b = 4.83 Å, c = 7.55 Å and β = 112.60°, which agreed well with the experimental values of a = 5.80 Å, b = 4.80 Å, c = 7.53 Å and β = 112.68° for CuP_2[62] (see Table 1).

3.2 Lattice transport properties

Lattice dynamics determines the dynamical stability of a crystalline solid with thermal vibration of constituent atoms at a given temperature. We first study harmonic phonon dispersion relations and phonon density of states (DOS) at T = 0 K. The convergence of phonon eigenvalues was checked with respect to the supercell size, showing that the results with a (2 × 2 × 2) supercell were almost identical to those with a (3 × 3 × 3) supercell (see Fig. S1, ESI†). Fig. 2(a) shows the calculated harmonic phonon dispersion relation (black dotted lines) of the monoclinic CuP_2 with space group $P2_1/c$. In the harmonic phonon dispersion, no anharmonic phonon modes with imaginary eigenvalues were found, indicating that CuP_2 stabilizes in the monoclinic phase under ambient conditions as reported in the previous experiments.[43,62]

We then performed SCP calculations at a finite temperature ranging from 100 K to 1000 K with a step of 100 K. After checking whether the temperature-dependent anharmonic effect appears in phonon dispersion, we performed anharmonic phonon renormalization at the whole range of phonon energy, so that there is no soft mode with imaginary phonon energy,[40,63] and compared it with the harmonic dispersions. We show the SCP dispersions and atom-projected phonon DOS calculated at 300 K representatively in Fig. 2(a) (see Fig. S2, ESI† for other dispersions at different temperatures). It was found from the

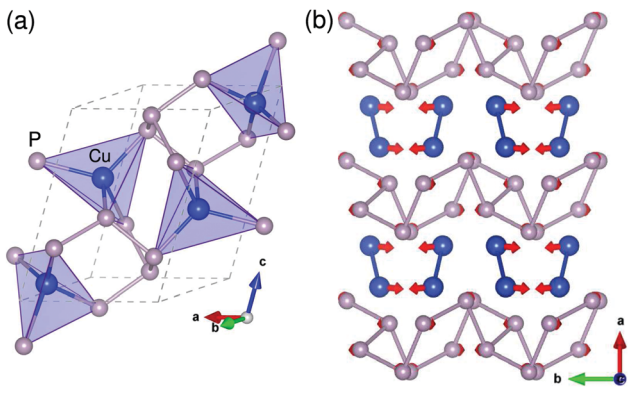

Fig. 1 (a) Polyhedral view of the crystal structure and (b) dimer rattling vibrations of Cu atoms corresponding to the lowest optical mode at the Γ point for monoclinic CuP_2 with the space group $P2_1/c$. Dashed lines indicate the unit cell and the red arrows represent the atomic displacement vectors.

Table 1 Lattice constants (*a*,*b*,*c*) and lattice angle (β), lattice thermal conductivity (κ_l), Seebeck coefficient (S) at a carrier concentration of 4.3 × 10^{17} cm^{-3}, figure of merit (ZT) at 300 K and band gap (E_g) for monoclinic CuP_2. Cal and Exp stand for calculation in this work and experiment in other works, respectively

Quantity	Cal.	Exp.
a,*b*,*c* (Å)	5.81, 4.83, 7.55	5.80, 4.80, 7.53[b]
β (deg)	112.60	112.68[b]
$\kappa_{l,xx}$, $\kappa_{l,yy}$, $\kappa_{l,zz}$ (W m^{-1} K^{-1})	2.81, 3.46, 3.49	3.57[c]
E_g (eV)	0.83, 1.19[a]	—
S_{xx}, S_{yy}, S_{zz} (μV K^{-1})	709, 659, 637	692[d]
n-ZT_x,ZT_y,ZT_z	0.13, 0.17, 0.10	—
p-ZT_x,ZT_y,ZT_z	0.34, 0.25, 0.14	—

[a] mBJ calculation and otherwise PBE calculation. [b] Ref. 62 [c] Ref. 43 [d] Ref. 42

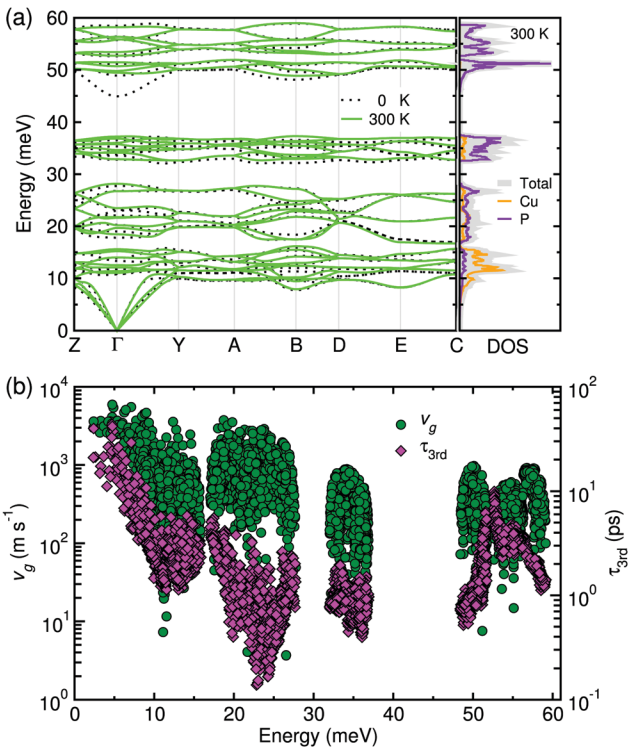

Fig. 2 (a) Harmonic phonon dispersion relation at T = 0 K (black dotted lines) and self-consistent phonon (SCP) dispersion relation (green solid lines) with the phonon density of states (DOS) at T = 300 K, and (b) phonon group velocity v_g and phonon lifetime τ_{3rd} as a function of phonon energy, estimated by SCP calculations at 300 K for CuP_2, calculated with the PBE functional.

phonon DOS at 300 K that the Cu atoms mainly contribute to the acoustic and low-energy optical modes below 15 meV, whereas the P atoms dominantly participate in the high-energy optical modes. This agrees well with previous work.[43] The vibrational behavior of the P atoms might be associated with much stronger covalent interactions among the P atoms and their lighter atomic mass when compared with the Cu-dimers. Meanwhile, the low-energy optical modes at the Γ point are related to a vibration of the Cu-dimers, exhibiting the flat dispersions at phonon energies from 11 to 15 meV. This indicates that the Cu-dimers originate the rattling modes (see Fig. 1(b)), *i.e.*, localized optical modes that reside near the acoustic modes and strongly scatter them with anti-crossing behavior in phonon dispersion.[43] The acoustic modes and low-energy optical modes are generally recognized to be the major contributors to lattice heat conduction,[43] and the rattling modes are known to play the key role in suppressing the lattice thermal conductivity.[64]

Using the self-consistent phonon dispersion relations and phonon DOS at different temperatures, we calculated the lattice transport properties of monoclinic CuP_2, such as phonon group velocity v_g, phonon lifetime τ_{3rd} and lattice thermal conductivity κ_l. With increasing temperature, the average v_g and τ_{3rd} were found to decrease monotonically owing to the enhancement of the phonon scattering intensity (see Fig. S3, ESI†). Fig. 2(b) shows the v_g and τ_{3rd} estimated from the SCP energies at 300 K. The phonon group velocity v_g at the Γ point was assessed to be about 6200 m s^{-1} at 300 K in good accordance with the sound speed of 6275 m s^{-1} observed at room temperature by Brillouin light scattering.[43] Such value of v_g for CuP_2 is relatively large, being about 3.5 times larger than those of PbTe (1780 m s^{-1}) and SnTe (1800 m s^{-1})[43] and thereby leading to higher thermal conductivity. On the other hand, the phonon lifetime τ_{3rd}, calculated by considering only the 3rd-order IFCs, was found to be below 50 ps, which is one order of magnitude smaller than that of PbTe in the previous calculation[65] and thus indicates a reduction of thermal conductivity. In particular, the τ_{3rd} rapidly decreases as the phonon energy increases from 0 to 15 meV, which might be due to the severe phonon scattering by the Cu-dimer rattling as mentioned above. Finally, we calculated the heat capacity C_V as a function of temperature, demonstrating that it follows the general tendency of a solid without any anomaly, as shown in Fig. 3(a). From these considerations, it is expected that CuP_2 in the monoclinic phase can exhibit ultralow lattice thermal conductivity at room temperature in spite of the considerably large sound velocity over 6000 m s^{-1}.

Given the calculated v_g, τ_{3rd} and C_V, we evaluated the lattice thermal conductivity κ_l within CRTA, using the formula $\kappa_l = \sum C_V |v_g|^2 \tau_{3rd}$. We carried out convergence testing for calculating the κ_l with respect to the size of the q-point mesh in the phonon BZ, demonstrating that the (20 × 20 × 16) mesh is sufficient to determine the κ_l with an error less than 0.03 W m^{-1} K^{-1} (see Fig. S4, ESI†). Fig. 3(a) displays the κ_l calculated with both the SCP (solid) and harmonic phonon (dashed) energies as increasing temperature. The κ_l computed with the harmonic phonon energies was found to be underestimated compared with the available experimental data,[43] which was already identified in the previous calculations.[59,65] After considering the temperature-dependent anharmonic effects with the SCP energies, the κ_l (*e.g.*, 3.49 W m^{-1} K^{-1} at 300 K) accords well with the experimental results (*i.e.*, 3.57 W m^{-1} K^{-1} at 300 K) for the CuP_2 in a single crystalline structure[43] (see Table 1). This lattice thermal conductivity is about a half of 6.96 W m^{-1} K^{-1} at 300 K for GeTe,[45] indicating that CuP_2 can be a very promising candidate for thermoelectric applications.

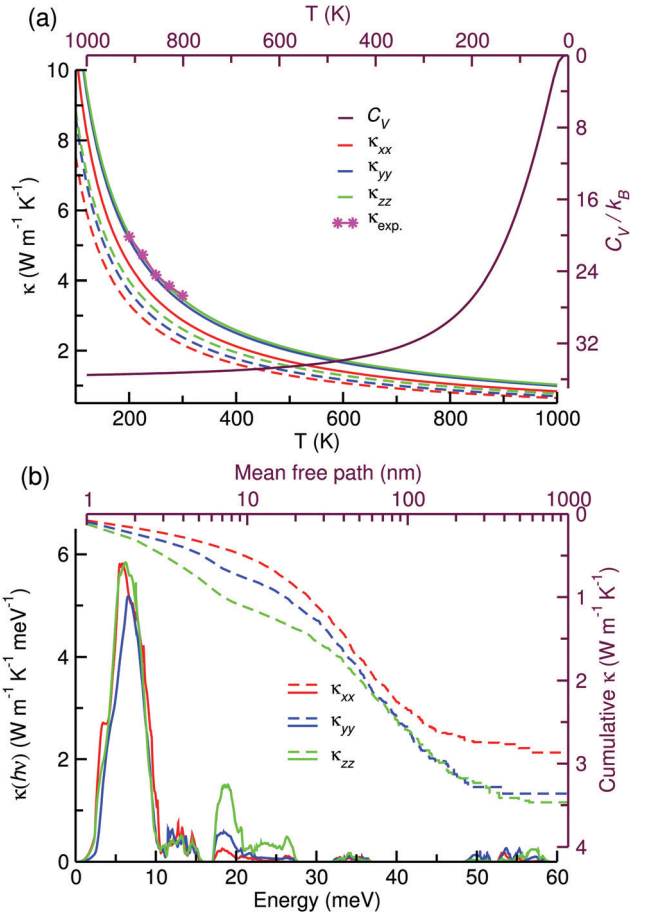

Fig. 3 (a) Lattice thermal conductivity κ_l and heat capacity C_V calculated on top of SCP (solid lines) and harmonic phonon (dashed lines) energies with experimental κ_l[43] as increasing temperature, and (b) thermal conductivity spectra $\kappa_l(h\nu)$ and cumulative κ_l at 300 K.

Fig. 3(b) shows the thermal conductivity spectra $\kappa_l(h\nu)$ as a function of phonon energy, and the cumulative κ_l as a function of mean free path (MFP), calculated at 300 K. From the figure, it was demonstrated that the acoustic and low-energy optical phonon modes below 11 meV dominantly contribute to the total κ_l, whereas the optical modes between 11 and 15 meV hardly contributes. The phonon modes in this region correspond to the Cu-dimer rattling vibrations, which significantly suppress the lattice thermal conductivity by strongly scattering the acoustic phonon. One can see from the top axis of Fig. 3(b) that the maximum MFP is about 450 nm and the major heat-carrying phonons have MFP ranging from 10 to 200 nm. It is worth noting that by nano-structuring, samples with a size less

than 50 nm can lower κ_l by half for CuP_2, which is even more positive for enhancing its thermoelectric performance.

3.3 Electronic structure

In order to gain insight into electron transport, we calculated the electronic band structure and DOS by the use of PBE and mBJ functionals for monoclinic CuP_2. Fig. 4(a) presents the PBE- and mBJ-calculated band structures. The transition of electrons from the valence band maximum (VBM) to the conduction band minimum (CBM) was found to possibly occur in an indirect way along the Γ – Y and Z – Γ lines of BZ. One can see that the mBJ calculations push up the conduction bands (CBs) as much as 0.37 eV in comparison with those by the PBE functional while the shift of the valence bands (VBs) is negligible, leading to widening of the band gap E_g from 0.83 to 1.19 eV. In order to assess the relativistic effect, we also took account of spin–orbit coupling in the calculation of electronic band structure, revealing that including SOC affects negligibly the band structure for CuP_2 because of the relatively light atomic masses of Cu and P elements (see Fig. S5, ESI† for comparison of the band structures with and without SOC effect).

For the characteristics of the band structure, the top VB and bottom CB are shown to be relatively flat along some BZ lines, *e.g.*, the E–C and A–B lines for the VB and CB respectively, while they are shown to be highly dispersive along all other directions. Moreover, it should be noted that both the VBs and CBs are doubly degenerated along the Y–A, D–E and E–C lines of BZ. Since it was demonstrated that in semiconductors the degenerated energy bands with a feature of being flat in one direction and highly dispersive in other directions lead to a high power factor,[66] the CuP_2 crystal can show a high power factor, thereby improving the thermoelectric performance. Fig. 4(b) shows the PBE- and mBJ-calculated total DOS, together with the atom-projected partial DOS obtained with the PBE functional. From the DOS analysis, both the VBs and CBs were found to be characterized by strong p–d hybridization between Cu 3d and P 3p states. This p–d hybridization is clearly shown in the inset of Fig. 4(b).

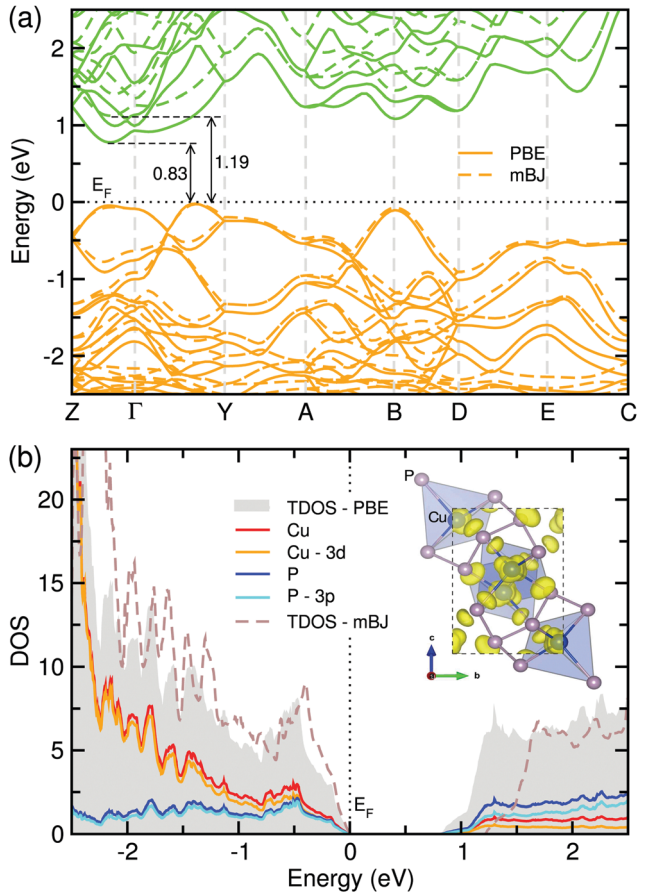

Fig. 4 (a) Electronic band structure calculated with the PBE (solid lines) and mBJ (dashed lines) functionals. Green and orange colors in the band structure indicate conduction and valence bands, respectively. (b) Total density of states (TDOS) and atom-projected partial DOS calculated with PBE and TDOS with mBJ. Black dotted lines mark the Fermi energy E_F. The inset shows the isosurface plot of charge density around the valence band maximum at a value of 0.03 |e| $Å^{-3}$.

3.4 Thermoelectric performance

Finally, we calculated the electronic transport properties, including the Seebeck coefficient S, electrical conductivity σ, power factor $S^2\sigma$ and electron thermal conductivity κ_e, by solving the electronic BTE within CRTA. The electronic band structure obtained with the mBJ functional was used as the input for solving the electronic BTE. We determined the relaxation time of an electron as increasing temperature by using eqn (2) (see Fig. S6, ESI†), where the coupling between the electronic bands and lattice vibrations corresponding to the acoustic phonon modes is considered by the deformation potential. Fig. 5 shows S and $S^2\sigma$ as functions of carrier concentration, calculated by using the PBE functional with the calculated relaxation time at T = 300, 500 and 700 K. At 300 K, the diagonal Cartesian components of the Seebeck coefficient, S_{xx}, S_{yy} and S_{zz} along the x-, y- and z-axes, were calculated to be 709, 659 and 637 μV K^{-1}, which agree well with the available experimental value of 692 μV K^{-1} observed at a carrier concentration of 4.3×10^{17} cm^{-3}.[42] Here, we used the prefix n- and p- for denoting the n- and p-type thermoelectric properties obtained upon n- and p-type doping, respectively. As can be seen in Fig. 5, the monoclinic CuP_2 has high p-type $S^2\sigma$ (n-type) values of 5.3 (4.7), 6.4 (5.8) and 7.4 (7.2) mW m^{-1} K^{-2} along the x-axis (y-axis) by optimizing the carrier concentration at 300, 500 and 700 K, respectively. These calculated values are comparable or even larger than the value of 3.3 mW m^{-1} K^{-2} at 700 K for the conventional TM GeTe.[11] Such high power factors are ascribed to the flat- and dispersive-band structures with high orbital degeneracy in CuP_2 as aforementioned in the analysis of electronic band structure.

At the end, we determined the figure of merit ZT as a function of carrier concentration by the use of the lattice transport and thermoelectric properties to gain insight into the thermoelectric performance of CuP_2, as shown in Fig. 5. We checked the calculation convergence using the different sets of k-point mesh as (24 × 24 × 16) and (20 × 20 × 12),

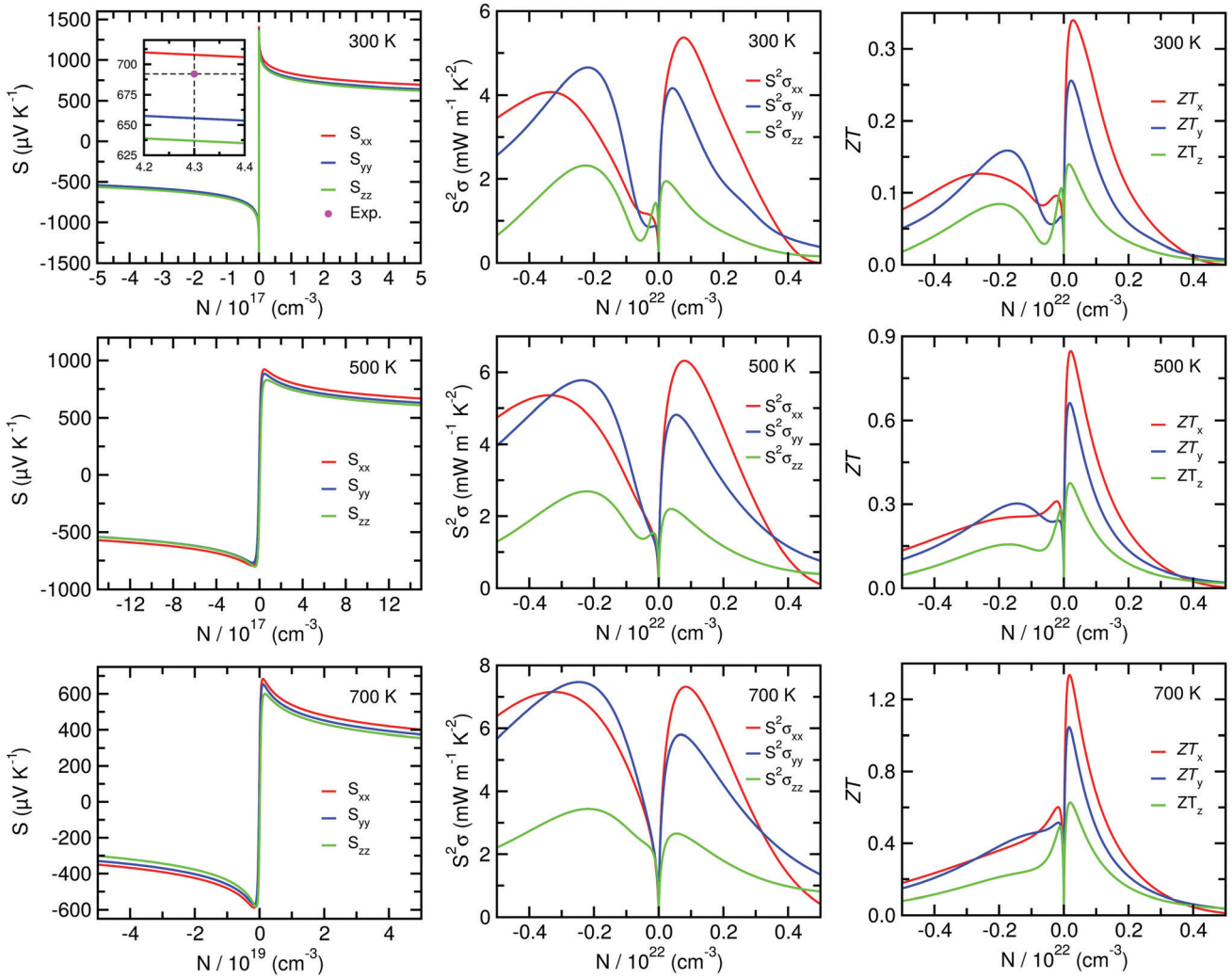

Fig. 5 Seebeck coefficient S (left panel), power factor $S^2\sigma$ (central panel) and figure of merit ZT (right panel) as functions of carrier concentration N, calculated with the PBE functional at T = 300 K (top panel), 500 K (middle panel) and 700 K (bottom panel) by setting the relaxation time as 10^{-14} s for monoclinic CuP_2. In the left-top panel for S at 300 K, the experimental value of 692 μV K^{-1} is marked.[42]

confirming the almost agreement between them (see Fig. S7, ESI†). From our calculations, it was found that the p-type doping exhibits more enhanced thermoelectric performance than the n-type doping at different temperatures considered in this work. Such a finding for CuP_2 does not change when using the mBJ functional instead of the PBE functional, although the ZT values with mBJ become lower or higher slightly for n- or p-type doping with increasing carrier concentration (see Fig. S8, ESI†). Upon increasing the temperature, the p-type ZT was found to be remarkably enhanced, such that ZT_x reaches over 1 at 700 K. At 700 K, the p-type ZT was found to reach the maximum values of 1.3 and 1.0 along the x- and y-axes at a carrier concentration of about 3×10^{20} cm^{-3}. In the previous experiment,[67] it was observed that without any external doping, the carrier concentration can reach a value of 1.7×10^{21} cm^{-3} maximizing the thermoelectric performance in metal phosphide NiP_2. Thus we can expect that the optimal carrier concentration of about 3×10^{20} cm^{-3} is reachable in CuP_2 for enhancing ZT. Table 1 summarizes the main resultant values for relevant quantities for monoclinic CuP_2 calculated in this work in comparison with the available experimental data. From the calculated values, the metal phosphide CuP_2 in the monoclinic phase can be said to be a promising material for highly efficient thermoelectric applications.

4 Conclusions

In this work, we have demonstrated excellent thermoelectric performance upon p-type doping onto metal phosphide CuP_2 in the monoclinic phase by using first-principles calculations based on the self-consistent phonon (SCP) theory and electron Boltzmann transport theory. Through the lattice dynamics calculations, we showed that CuP_2 exhibits an unusually low lattice thermal conductivity κ_l below 3.6 W m^{-1} K^{-1} at 300 K, even though it shows a large sound speed over 6200 m s^{-1}, revealing that such low κ_l is most likely due to Cu-dimer rattling modes that strongly scatter the heat-carrying acoustic and

low-energy optical phonons. Moreover, CuP_2 was predicted to have a high power factor $S^2\sigma$ of 5.3, 6.4 and 7.4 mW m^{-1} K^{-2} upon p-type doping at 300, 500 and 700 K, being superior to the value of 3.3 mW m^{-1} K^{-2} of GeTe at 700 K. These low κ_l and high $S^2\sigma$ were found to yield an ultrahigh figure of merit ZT of 1.3 at 700 K by optimizing the hole concentration as $\sim 3 \times 10^{20}$ cm^{-3}. We believe that our work offers a new way for discovering and designing novel thermoelectric materials based on the metal phosphide CuP_2, emphasizing that a promising route for further enhancing ZT is to reduce lattice thermal conductivity by nanostructuring or dimension-lowering.

Author contributions

Un-Gi Jong developed the original project and performed the calculations and drafted the first manuscript. Chol-Hyok Ri, Chol-Jin Pak and Chol-Hyok Kim assisted with the DFT calculations and contributed to useful discussions. Stefaan Cottenier and Chol-Jun Yu supervised the work. All authors reviewed the manuscript.

Conflicts of interest

There are no conflicts to declare.

Acknowledgements

This work is supported as part of the basic research project ''Design of New Energy Materials'' (No. 2021-12) funded by the State Commission of Science and Technology, DPR Korea. Computations have been performed on the HP Blade System C7000 managed by the Faculty of Materials Science, Kim Il Sung University.

References

1 L. E. Bell, *Science*, 2008, **321**, 1457–1461.
2 G. Tan, F. Shi, S. Hao, H. Chi, L. D. Zhao, C. Uher, C. Wolverton, V. P. Dravid and M. G. Kanatzidis, *J. Am. Chem. Soc.*, 2015, **137**, 5100–5112.
3 G. Guelou, P. Lemoine, B. Raveau and E. Guilmeau, *J. Mater. Chem. C*, 2021, **9**, 773–795.
4 A. Suwardi, S. H. Lim, Y. Zheng, X. Wang, S. W. Chien, X. Y. Tan, Q. Zhu, L. Mun, N. Wang, J. Cao, W. Wang, Q. Yan, C. K. I. Tan and J. Xu, *J. Mater. Chem. C*, 2020, **8**, 16940–16948.
5 G. J. Snyder and E. S. Toberer, *Nat. Mater.*, 2008, **7**, 105.
6 M. Oudah, K. M. Kleinke and H. Kleinke, *Inorg. Chem.*, 2015, **54**, 845–849.
7 H. Chen, H. Lin, Z.-X. Lin, J.-N. Shen, L. Chen and L.-M. Wu, *Inorg. Chem.*, 2015, **54**, 867–871.
8 Y. Gelbstein and J. Davidow, *Phys. Chem. Chem. Phys.*, 2014, **16**, 20120–20126.
9 Y. Pei, J. Lensch-Falk, E. S. Toberer, D. L. Medlin and G. J. Snyder, *Adv. Funct. Mater.*, 2011, **21**, 241–249.
10 Y. Pei, A. F. May and G. J. Snyder, *Adv. Energy Mater.*, 2011, **21**, 291–296.
11 M. Hong, Z.-G. Chen, L. Yang, Y.-C. Zou, M. S. Dargusch, H. Wang and J. Zou, *Adv. Mater.*, 2018, **30**, 1705942.
12 Q. Wang, L. Yang, S. Zhou, X. Ye, Z. Wang, W. Zhu, M. D. McCluskey and Y. Gu, *J. Phys. Chem. Lett.*, 2017, **8**, 2887–2894.
13 H. J. Wu, L. D. Zhao, F. S. Zheng, D. Wu, Y. L. Pei, X. T. M. G. Kanatzidis and J. Q. He, *Nat. Commun.*, 2014, **5**, 4515.
14 L. D. Zhao, S. H. Lo, Y. Zhang, H. Sun, G. Tan, C. Uher, C. Wolverton, V. P. Dravid and M. G. Kanatzidis, *Nature*, 2014, **508**, 373–377.
15 S. Forbes, Y.-C. Tseng and Y. Mozharivskyj, *Inorg. Chem.*, 2015, **54**, 815–820.
16 O. Cherniushok, R. Cardoso-Gil, T. Parashchuk, Y. Grin and K. T. Wojciechowski, *Inorg. Chem.*, 2021, **60**, 2771–2782.
17 F. Mehmood, H. Wang, W. Su, M. Khan, T. Huo, T. Chen, G. Chebanova, A. Romanenko and C. Wang, *Inorg. Chem.*, 2021, **60**, 3452–3459.
18 V. L. Kuznetsov, L. A. Kuznetsova, A. E. Kaliazin and D. M. Rowe, *J. Mater. Sci.*, 2002, **37**, 2893–2897.
19 X. Guo, J. Qin, X. Lv, L. Deng, X. Jia, H. Ma and H. Jia, *RSC Adv.*, 2016, **6**, 60736–60740.
20 R. Deng, X. Su, Z. Zheng, W. Liu, Y. Yan and Q. Zhang, *Sci. Adv.*, 2018, **4**, eaar5606.
21 S. Fan, J. Zhao, J. Guo, Q. Yan, J. Ma and H. H. Hong, *Appl. Phys. Lett.*, 2010, **96**, 182104.
22 Q. Jiang, H. Yan, J. Khaliq, H. Ning, S. Grasso, K. Simpsonb and M. J. Reece, *J. Mater. Chem. A*, 2014, **2**, 5785–5790.
23 T. Zhu, Z. Xu, J. He, J. Shen, S. Zhu, L. Hu, T. Tritt and X. Zhao, *J. Mater. Chem. A*, 2013, **1**, 11589–11594.
24 Y. Ma, Q. Hao, B. Poudel, Y. Lan, B. Yu, D. Wang, G. Chen and Z. Ren, *Nano Lett.*, 2008, **8**, 2580–2584.
25 L. P. Hu, H. Gao, X. Liu, H. H. Xie, J. Shen, T. J. Zhu and X. B. Zhao, *J. Mater. Chem.*, 2012, **22**, 16484–16490.
26 Y. Qiu, J. Xing, X. Gao, L. Xi, X. Shi, H. Gu and L. Chen, *J. Mater. Chem. A*, 2014, **2**, 10952.
27 X. Shi, J. Yang, J. R. Salvador, M. Chi, J. Y. Cho, H. Wang, S. Q. Bai, J. Yang, W. Zhang and L. Chen, *J. Am. Chem. Soc.*, 2011, **133**, 7837.
28 Y. Tang, Z. M. Gibbs, L. A. Agapito, G. Li, H. S. Kim, M. S. Nardelli, S. Curtarolo and G. J. Snyder, *Nat. Mater.*, 2015, **14**, 1223.
29 X. Zhou, G. Wang, L. Zhang, H. Chi, X. Su, J. Sakamoto and C. Uher, *J. Mater. Chem.*, 2012, **22**, 2958.
30 A. Gharleghi, Y. H. Chu, F. H. Lin, Z. R. Yang, Y. H. Pai and C. J. Liu, *ACS Appl. Mater. Interfaces*, 2016, **8**, 5205–5215.
31 C. A. Uvarov, F. O. Alvarez and S. M. Kauzlarich, *Inorg. Chem.*, 2012, **51**, 7617–7624.
32 A. Miura, S. Zhou, T. Nozaki and J. Shiomi, *ACS Appl. Mater. Interfaces*, 2015, **7**, 13484–13489.
33 J. Tang, H. T. Wang, D. H. Lee, M. Fardy, Z. Huo, T. P. Russell and P. Yang, *Nano Lett.*, 2010, **10**, 4279–4283.
34 J. He, S. Hao, Y. Xia, S. S. Naghavi, V. Ozolins and C. Wolverton, *Chem. Mater.*, 2017, **29**, 2529–2534.

35 Z. Li, C. Xiao, S. Fan, Y. Deng, W. Zhang, B. Ye and Y. Xie, *J. Am. Chem. Soc.*, 2015, **137**, 6587–6593.
36 W. Rahim, J. M. Skelton and D. O. Scanlon, *J. Mater. Chem. A*, 2020, **8**, 16405–16420.
37 A. Ramanathan, J. E. Leisen and H. S. L. Pierre, *Inorg. Chem.*, 2021, **60**, 1398–1410.
38 U.-G. Jong, C.-J. Yu, Y.-H. Kye, S.-N. Hong and H.-G. Kim, *Phys. Rev. Mater.*, 2020, **4**, 075403.
39 Q. Feng, H. Mingyu, G. Jue, G. Chunyu, Z. Yunzuen, G. Jun, C. Min, G. Zhenhua, P. Nitin, Z. Yuanyuan and F. Jing, *J. Phys. Chem. C*, 2020, **124**, 11749–11753.
40 U.-G. Jong, Y.-S. Kim, C.-H. Ri, Y.-H. Kye and C.-J. Yu, *J. Phys. Chem. C*, 2021, **125**, 6013–6019.
41 X. Shen, Y. Xia, G. Wang, F. Zhou, V. Ozolins, X. Lu, G. Wang and X. Zhou, *J. Mater. Chem. A*, 2018, **6**, 24877–24884.
42 J. P. Odile, S. Soled, C. A. Castro and A. Wold, *Inorg. Chem.*, 1978, **17**, 283–286.
43 J. Qi, B. Dong, Z. Zhang, Z. Zhang, Y. Chen, Q. Zhang, S. Danilkin, X. Chen, J. He, L. Fu, X. Jiang, G. Chai, S. Hiroi, K. Ohara, Z. Zhang, W. Ren, T. Yang, J. Zhou, S. Osami, J. He, D. Yu, B. Li and Z. Zhang, *Nat. Commun.*, 2020, **11**, 5197.
44 A. Olvera, G. Shi, H. Djieutedjeu, A. Page, C. Uher, E. Kioupakis and P. F. P. Poudeu, *Inorg. Chem.*, 2015, **54**, 746–755.
45 B. Srinivasan, C. Boussard-Pledel and B. Bureau, *Mater. Lett.*, 2018, **230**, 191–194.
46 S. Perumal, P. Bellare, U. S. Shenoy, U. V. Waghmare and K. Biswas, *Chem. Mater.*, 2017, **29**, 10426.
47 G. Kresse and J. Furthmüller, *Comput. Mater. Sci.*, 1996, **6**, 15–50.
48 G. Kresse and J. Furthmüller, *Phys. Rev. B: Condens. Matter Mater. Phys.*, 1996, **54**, 11169–11186.
49 P. E. Blöchl, *Phys. Rev. B: Condens. Matter Mater. Phys.*, 1994, **50**, 17953–17979.
50 G. Kresse and D. Joubert, *Phys. Rev. B: Condens. Matter Mater. Phys.*, 1999, **59**, 1758–1775.
51 J. P. Perdew, K. Burke and M. Ernzerhof, *Phys. Rev. Lett.*, 1996, **77**, 3865.
52 F. Tran and P. Blaha, *Phys. Rev. Lett.*, 2009, **102**, 226401.
53 J. Heyd, G. E. Scuseria and M. Ernzerhof, *J. Chem. Phys.*, 2003, **118**, 8207–8215.
54 M. Shishkin and G. Kresse, *Phys. Rev. B: Condens. Matter Mater. Phys.*, 2007, **75**, 235102.
55 J. Xi, M. Long, L. Tang, D. Wang and Z. Shuai, *Nanoscale*, 2012, **4**, 4348.
56 H. Wang, Y. Pei, A. D. LaLonde and G. J. Snyder, *Proc. Natl. Acad. Sci. U. S. A.*, 2012, **109**, 9709.
57 K. H. Madsen, J. Carrete and M. J. Verstraete, *Comput. Phys. Commun.*, 2018, **231**, 140–145.
58 T. Tadano, Y. Gohda and S. Tsuneyuki, *J. Phys.: Condens. Matter*, 2014, **26**, 225402.
59 T. Tadano and S. Tsuneyuki, *Phys. Rev. B: Condens. Matter Mater. Phys.*, 2015, **92**, 054301.
60 F. Zhou, W. Nielson, Y. Xia and V. Ozolins, *Phys. Rev. Lett.*, 2014, **113**, 185501.
61 Y. Xia, J. M. Hodges, M. G. Kanatzidis and M. K. Y. Chan, *Appl. Phys. Lett.*, 2018, **112**, 181906.
62 M. H. Moeller and W. Jeitschko, *Z. Anorg. Allg. Chem.*, 1982, **491**, 225–236.
63 Y. Xia and M. K. Y. Chan, *Appl. Phys. Lett.*, 2018, **113**, 193902.
64 W. Lee, H. Li, A. B. Wong, D. Zhang, M. Lai, Y. Yu, Q. Kong, E. Lin, J. J. Urban, J. C. Grossman and P. Yang, *Proc. Natl. Acad. Sci. U. S. A.*, 2017, **114**, 8693–8697.
65 Y. Xia, *Appl. Phys. Lett.*, 2018, **113**, 073901.
66 D. I. Bilc, G. Hautier, D. Waroquiers, G. M. Rignanese and P. Ghosez, *Phys. Rev. Lett.*, 2015, **114**, 136601.
67 J.-H. Pohls, A. Faghaninia, G. Petretto, U. Aydemir, F. Ricci, G. Li, M. Wood, S. Ohno, G. Hautier, G. J. Snyder, G.-M. Rignanese, A. Jain and M. A. White, *J. Mater. Chem. C*, 2017, **5**, 12441.

